Check for updates

JGR Atmospheres

RESEARCH ARTICLE
10.1029/2024JD042239

Impact of Large-Scale Topography Surrounding the Sichuan Basin on Its Regional Hourly Extreme Precipitation in Summer Under Specific Weather Patterns: Multi-Case Study

Xiaoke Xu[1,2], Anning Huang[2,3], Yan Zhang[4], Xianyu Yang[3], and Wei Zhao[5]

[1]Chongqing Jinfo Mountain Karst Ecosystem National Observation and Research Station, Chongqing Engineering Research Center for Remote Sensing Big Data Application, School of Geographical Sciences, Southwest University, Chongqing, China, [2]School of Atmospheric Sciences, Nanjing University, Nanjing, China, [3]Plateau Atmosphere and Environment Key Laboratory of Sichuan Province, College of Atmospheric Sciences, Chengdu University of Information Technology, Chengdu, China, [4]Key Laboratory of Radiometric Calibration and Validation for Environmental Satellites, National Satellite Meteorological Center, FengYun Meteorological Satellite Innovation Center (FY-MSIC), China Meteorological Administration (LRCVES/CMA), Beijing, China, [5]Nanjing Institute of Environmental Sciences, Ministry of Ecology and Environment of the People's Republic of China, Nanjing, China

Key Points:

- Large-scale topography surrounding the Sichuan Basin (SCB) determines the occurrence and positions of its regional hourly extreme precipitation event (RHEPE) under specific weather patterns
- Under the influence of the two primary weather patterns, the Tibetan Plateau amplifies the RHEPE precipitation within the SCB
- The Yunnan–Guizhou Plateau exerts opposite impact on the precipitation in SCB under the two dominant weather patterns of RHEPE

Correspondence to:
A. Huang,
anhuang@nju.edu.cn

Citation:
Xu, X., Huang, A., Zhang, Y., Yang, X., & Zhao, W. (2025). Impact of large-scale topography surrounding the Sichuan Basin on its regional hourly extreme precipitation in summer under specific weather patterns: Multi-case study. *Journal of Geophysical Research: Atmospheres*, *130*, e2024JD042239. https://doi.org/10.1029/2024JD042239

Received 14 AUG 2024
Accepted 16 APR 2025

Author Contributions:
Conceptualization: Xiaoke Xu, Anning Huang, Yan Zhang
Data curation: Xiaoke Xu
Formal analysis: Xiaoke Xu, Anning Huang
Investigation: Xiaoke Xu, Anning Huang
Methodology: Xiaoke Xu, Anning Huang, Yan Zhang, Xianyu Yang
Resources: Xiaoke Xu
Software: Xiaoke Xu, Anning Huang, Xianyu Yang
Supervision: Anning Huang, Yan Zhang
Validation: Xiaoke Xu, Anning Huang, Wei Zhao
Writing – original draft: Xiaoke Xu, Anning Huang, Yan Zhang, Xianyu Yang, Wei Zhao
Writing – review & editing: Xiaoke Xu, Anning Huang, Yan Zhang, Xianyu Yang, Wei Zhao

© 2025. American Geophysical Union. All Rights Reserved.

Abstract The influence mechanism of large-scale topography surrounding the Sichuan Basin (SCB) on its precipitation under two dominant weather patterns that typically trigger the regional hourly extreme precipitation events (RHEPEs) in summer remains unclear. Based on multi-case simulations, this study revealed how the Tibetan Plateau (TP) and Yunnan–Guizhou Plateau (YGP) affect the precipitation over SCB under different dominant weather patterns of RHEPEs in summer through sensitivity experiments. Results show that under the weather pattern featured by a low-level vortex (LLV) over western SCB with water vapor transport by southerly winds, the YGP and TP can increase the precipitation in western SCB by 86% and 46%, respectively. The large-scale terrains of TP and YGP tend to enhance the thermal gradient between the plateau and basin and shape the windward slope over western SCB, accounting for increased precipitation there. Under the weather pattern featured by a LLV over central and eastern SCB with southwesterly winds, the TP can only increase the precipitation in the eastern SCB by 20% due to its limited effects on the atmospheric circulations along the windward slope there, however, the YGP can decrease the precipitation in eastern SCB by 26%, which is attributed to the anomalous northeasterly winds weakening the water vapor transport from the Bay of Bengal, leading to the strengthened stability of stratification and weakened dynamic uplifting along the windward slope in eastern SCB. Finding of this study provides a new perspective on the mechanisms of large-scale terrain influencing the RHEPEs over SCB.

Plain Language Summary How the large-scale terrain surrounding Sichuan Basin (SCB) affects its regional hourly extreme precipitation events (RHEPEs) under different weather patterns is still unclear. This study designs sensitivity experiments by removing the Tibetan Plateau (TP) or Yunnan–Guizhou Plateau (YGP) to answer this question. Results show that under the two dominant weather patterns that typically trigger the RHEPEs in summer over SCB, TP tends to increase the precipitation in SCB by strengthening the thermal gradient between the basin and plateau. However, the YGP exhibits the opposite impact on the precipitation in SCB under the two dominant weather patterns. This study provides insights that enhance the comprehension of how the surrounding large-scale topography affects the RHEPEs over the SCB under different weather patterns.

1. Introduction

Regional hourly extreme precipitation events (RHEPEs) induced by specific weather patterns are different from local extreme precipitation events with the characteristics of wide influence and strong disasters (Li et al., 2021; Ng et al., 2021; Xu et al., 2023; Zeng et al., 2023). In recent years, extreme precipitation events have increased significantly in China amidst the context of global warming (Chang et al., 2020; Luo et al., 2016; Zheng et al., 2019). Particularly, the RHEPEs in Sichuan Basin (SCB) surrounded by the TP and YGP occur frequently due to the complex terrain under favorable weather patterns (Nie & Sun, 2021; Xu et al., 2023; Zhang et al., 2019,

21698996, 2025, 9, Downloaded from https://agupubs.onlinelibrary.wiley.com/doi/10.1029/2024JD042239 by Anming Huang - Nanjing University , Wiley Online Library on [28/04/2025]. See the Terms and Conditions (https://onlinelibrary.wiley.com/terms-and-conditions) on Wiley Online Library for rules of use; OA articles are governed by the applicable Creative Commons License

2021). It is necessary to clearly understand how the large-scale topography affects the RHEPEs in SCB under different weather patterns.

Large-scale topography is a key extrinsic forcing factor affecting extreme precipitation (Ge et al., 2017; Tang et al., 2018; Wu et al., 2022; Xu et al., 2024; Yang et al., 2022). The Mountain–plains solenoid formed by the thermal gradient between large-scale topography and surrounding plain promotes nonadiabatic heating over the plain region, which intensifies the instability of the lower troposphere and triggers the mesoscale convective system (Bao et al., 2011; Chen et al., 2016; Hua et al., 2020; Jin et al., 2013; Pan & Chen, 2019; Sun & Zhang, 2012). In addition, the dynamic uplifting and blocking effects of large-scale terrain in the windward slope to the air can strengthen the precipitation intensity and further promote the generation of RHEPEs (Almazroui et al., 2018; Nielsen et al., 2016; Wu & Li, 2022; Xu & Yao, 2015).

The TP is the most important large-scale topography around the SCB. Its dynamic and thermal effects can not only determine the formation of South Asia High (SAH) but also influence the location and intensity of West North Pacific Subtropical High (WNPSH) and the East Asian summer monsoon intensity (Duan et al., 2012; Ma et al., 2022; Qiao et al., 2022; Wu et al., 2015; Wu & Li, 2022; Xia et al., 2021). Moreover, the south branches of westerly wind flow shaped by the TP and the eastward-extension plateau trough together form the southwest vortex (SWV) (Fu et al., 2020; Wang & Tan, 2014; Yang et al., 2023), which is the most important weather system causing extreme rainfall in SCB (Dong et al., 2022; Li & Zhang, 2023). In addition, YGP is the second-largest large-scale topography around the SCB. The mechanical blocking of YGP on the southwest monsoon, the tropical easterly winds, and mid-latitude westerly winds are crucial to the formation of the SWV and water vapor transportation to the SCB (Cheng et al., 2016; Shi et al., 2019; Yang et al., 2023). Analogously, the YGP also forms a thermal gradient with SCB and further affects the precipitation in this area (Jin et al., 2013; Yang et al., 2023).

In addition to the terrain, the favorable weather pattern is another indispensable factor in the occurrence of RHEPEs (Tang et al., 2021; Zeng et al., 2023; Zhang et al., 2021). Previous researches pointed out that weather patterns controlling the RHEPEs over the SCB in summer can be divided into two categories: (a) The northeastward-extended SAH, northern westward-extended WNPSH, and the low-level vortex (LLV) in the central and western SCB with the water vapor transport of southerly winds (Hu et al., 2015; Nie & Sun, 2021; Xu et al., 2023; Zhang et al., 2021). (b) The southeastward-extended SAH, southwestward-extended WNPSH, and the central and eastern SCB with the water vapor transport of southwesterly winds (Liu et al., 2022; Xu et al., 2023). Under the above-mentioned circulation background, the shear lines, topographic troughs, and other middle-small scale weather systems superimposed local topography together aggravate the frequency of RHEPEs in summer over the SCB (Li et al., 2023; Luo et al., 2016; Xia et al., 2021). It can be seen that the advantageous circulation background and terrain are equally critical to the occurrence and development of RHEPEs.

Previous studies have obtained a certain recognition of the dominant weather patterns that typically trigger the RHEPEs in summer over SCB, and exposed how large-scale topography affects local convective systems and further affects extreme rainfall in SCB (Hu et al., 2015; Jin et al., 2013; Liu et al., 2022; Nie & Sun, 2021; Xia et al., 2021; Xu et al., 2023). However, these studies mostly focused on a single case and a single circulation background to discuss the influence of large-scale topography on extreme precipitation (Ma et al., 2022; Qian et al., 2022; Wu & Li, 2022; Xia et al., 2021; Zhang & Sun, 2021). Under different circulation backgrounds, the leeward and windward slopes induced by the large-scale topography are different. It is worth deeply pondering whether the same large-scale topography has the same influence mechanism on RHEPEs under different weather patterns.

To address this issue, this study selected ten typical cases of RHEPEs in each weather pattern to reveal how the large-scale terrains surrounding SCB affect its RHEPEs under different weather patterns. Following Xu et al. (2023), the precipitation intensity and occurrence range of the twenty cases are consistent with the definition of RHEPE and the twenty cases happened under two completely different weather patterns. This study designs sensitivity experiments by flattening large-scale topography (TP and YGP) around the SCB and answers the following questions: (a) What is the influence mechanism of the large-scale topography (TP and YGP) on the RHEPEs in SCB under different dominant weather patterns? (b) Does the same large-scale topography exert a uniform influence on the RHEPEs in SCB across different weather patterns? This study provides a new perspective on the effect of large-scale topography on extreme rainfall.

21698996, 2025, 9, Downloaded from https://agupubs.onlinelibrary.wiley.com/doi/10.1029/2024JD042239 by Aiming Huang - Nanjing University , Wiley Online Library on [28/04/2025]. See the Terms and Conditions (https://onlinelibrary.wiley.com/terms-and-conditions) on Wiley Online Library for rules of use; OA articles are governed by the applicable Creative Commons License

Table 1
Time of the RHEPE Cases Selected in This Study

P1 cases	P2 cases
07:00 BJT on 07 August–08:00 BJT on 08 August 2001	15:00 BJT on 18 July–06:00 BJT on 19 July 2003
12:00 BJT on 29 August–06:00 BJT on 30 August 2003	07:00 BJT on 27 June–02:00 BJT on 28 June 2009
16:00 BJT on 04 July–18:00 BJT on 05 July 2007	12:00 BJT on 16 June–05:00 BJT on 17 June 2011
12:00 BJT on 20 July–09:00 BJT on 21 July 2008	10:00 BJT on 23 June–05:00 BJT on 24 June 2016
12:00 BJT on 24 July–02:00 BJT on 25 July 2010	05:00 BJT on 30 June–22:00 BJT on 30 June 2016
12:00 BJT on 08 August–04:00 BJT on 09 August 2014	11:00 BJT on 07 August–03:00 BJT on 08 August 2017
19:00 BJT on 01 July–23:00 BJT on 02 July 2018	15:00 BJT on 21 June–06:00 BJT on 22 June 2019
17:00 BJT on 21 July–07:00 BJT on 22 July 2019	12:00 BJT on 26 June–09:00 BJT on 27 June 2020
10:00 BJT on 15 August–05:00 BJT on 16 August 2020	21:00 BJT on 26 July–05:00 BJT on 17 July 2020
20:00 BJT on 10 August–03:00 BJT on 13 August 2020	11:00 BJT on 25 July–05:00 BJT on 26 July 2020

2. Background, Data, Numerical Design, and Methodology

2.1. Definition of Regional Hourly Extreme Precipitation Events

The RHEPEs are detected by the method of Xu et al. (2023) as follows: The extreme precipitation threshold at each grid in the SCB is determined as the 95th percentile of all historical hourly precipitation records with an intensity ≥0.1 mm in the summers of 2000–2020. The grid number threshold of RHEPEs is defined as the 95th percentile of grid number with concurrent occurrence of extreme precipitation over the SCB in the summers of 2000–2020. In this study, we selected the RHEPEs with a duration exceeding 12 hr under two dominant weather patterns (Table 1). Overall, under a given weather pattern the selected cases can correspond well with the spatial distribution of total RHEPEs under this weather pattern (not shown).

2.2. Background

Sichuan Basin is one of the four major basins in China, bordering TP to the west and YGP to the south (Figures 1a and 1b). Due to the special topographic distribution, the RHEPEs dominate the total extreme precipitation in summer over SCB, and it is mainly dominated by the two types of weather patterns (Xu et al., 2023). Therefore, ten typical RHEPEs in each weather pattern are selected in this work, which have different configurations containing the atmospheric circulation systems at different levels and water vapor transport. More details of the twenty RHEPE cases are shown as follows: The mean precipitation of the ten cases under the weather pattern 1 (P1) distributed in the western SCB with a rainfall center exceeding 100 mm. The P1 is featured by the north-eastward (northwestward) extension of SAH (WNPSH) relative to its climatology, a LLV at 850 hPa over western SBC, and the prevailing water vapor transport of southerly winds along the west edge of WNPSH (Figure 1c). Under P1, the large-scale topography (TP and YGP) and the LLV at 850 hPa over the western SCB with the easterly winds in the lower troposphere shape the windward slope in the western SCB (Figure 1e). The mean precipitation of ten cases under the weather pattern 2 (P2) mainly concentrates on the central-eastern SCB with a rainfall center exceeding 90 mm. The P2 is characterized by the configurations of the eastward (southwestward) extension of SAH (WNPSH) relative to its climatology, the LLV in the central SCB over 850 hPa and the prevailing water vapor transport of southwesterly winds along the north edge of WNPSH (Figure 1d). Under P2, the terrain along the eastern edge of SCB combines the LLV at 850 hPa over the central SCB conducting the prevailing westerly winds over the eastern SCB at the lower troposphere, which shapes the windward slope along the eastern edge of SCB (Figure 1f). As the prevailing wind direction and the location of the windward slope in the lower troposphere are different under different weather patterns, it needs further investigation on the terrain effect on the formation of RHEPEs under different weather patterns.

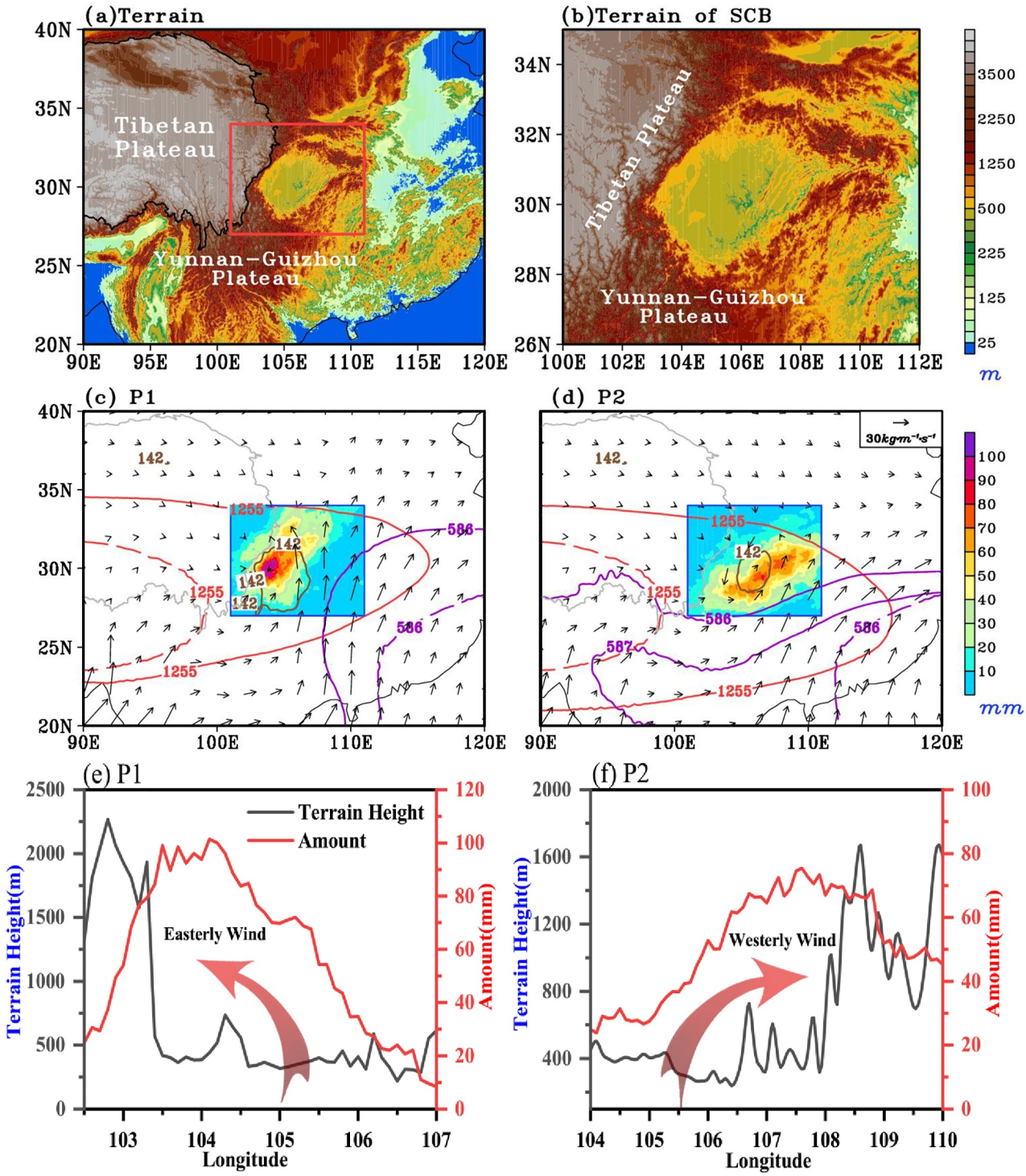

Figure 1. The terrain height of the study area (a, b). Spatial distribution of the composite mean precipitation (shading, unit: mm) and vertically integrated water vapor flux from surface to 300 hPa (vector, unit: $kg \cdot m^{-1} \cdot s^{-1}$) and configurations of atmospheric circulation at different levels for the 10 selected regional hourly extreme precipitation event cases under each weather pattern (c, d), including the South Asia High at 200 hPa (climatology: red dotted lines, weather pattern: red solid lines), West North Pacific Subtropical High at 500 hPa (climatology: purple dotted lines, weather pattern: purple solid lines), low-level vortex at 850 hPa (brown line) in panels (c) and (d). The climatology represents the mean geopotential height in the summers of 2000–2020. The blue squares in panels (c) and (d) denote the Sichuan Basin (SCB). The variation of terrain height (black line, unit: m) and precipitation amount (red line, unit: mm) with longitude along the 30°N under the dominant weather patterns P1 (e) and P2 (f). The red arrows symbolize the different prevailing winds under different weather patterns over the SCB.

21698996, 2025, 9, Downloaded from https://agupubs.onlinelibrary.wiley.com/doi/10.1029/2024JD042239 by Aiming Huang - Nanjing University , Wiley Online Library on [28/04/2025]. See the Terms and Conditions (https://onlinelibrary.wiley.com/terms-and-conditions) on Wiley Online Library for rules of use; OA articles are governed by the applicable Creative Commons License

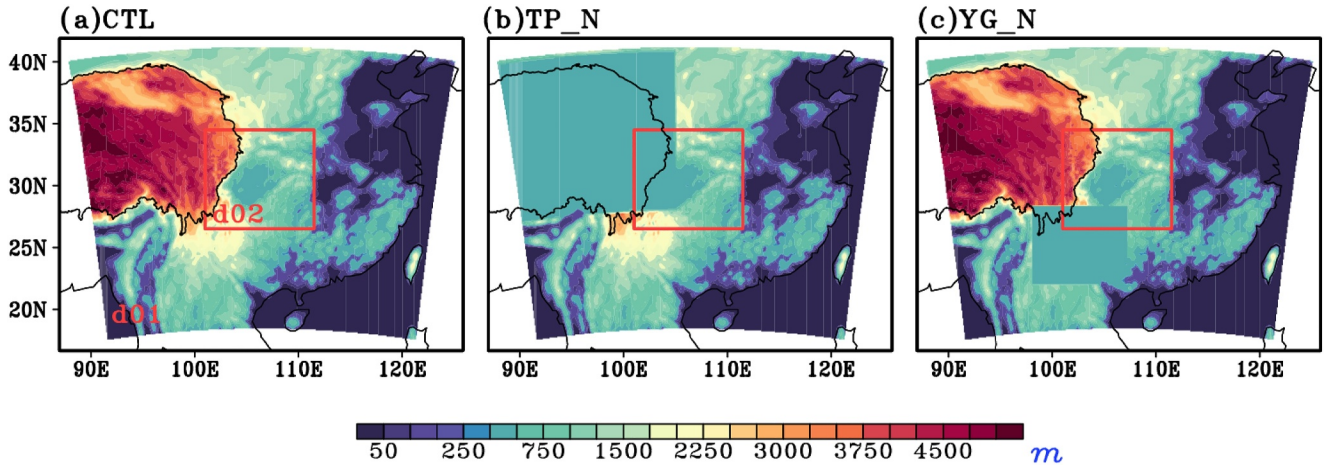

Figure 2. The nesting strategy used in the WRF model and terrain distribution of the CTL experiment and each sensitivity experiment. Shading represents the altitude representing the real topography in the CTL experiment (a), the designed topography of the TP_N experiment without Tibetan Plateau (27°N–40°N, 85°E–104.5°E) (b), the designed topography of the YG_N experiment without Yunnan–Guizhou Plateau (22°N–28°N and 98°E–107°E) (c).

2.3. Data

The following is a list of the data utilized in this study.

1. The six hourly FNL global reanalysis data with the horizontal resolutions of 1° × 1° at 26 pressure levels in the vertical direction, which is used to drive the numerical model (Huang & Gao, 2018).
2. The hourly ERA5 reanalysis data with the 0.25° horizontal resolution covering the twenty RHEPEs in this study (Table 1), which is adopted to judge the ability of the model in the simulation of the atmospheric circulations (Hersbach et al., 2020).
3. The precipitation data of the final run GPM-IMERG V06 with the time-resolution of the half-hourly and horizontal resolution of 0.1° × 0.1° covering the twenty RHEPEs in this study (Table 1), which are employed to assess the accuracy of the model in replicating the precipitation. Previous research has confirmed that this data is capable of accurately capturing the spatial and temporal distribution and magnitude of extreme rainfall events across the SCB (Fang et al., 2019; Shen et al., 2022; Yang et al., 2020).

2.4. Numerical Experimental Design

This study used the WRF4.2 model released by the NCAR (Skamarock et al., 2019). The model strategy adopted in this work is the two-way nest by the first (second) layer with a horizontal resolution of 18 (6) km and domain at 41 vertical levels (Figure 2a). The domain is centered at 29.83°N, 106.46°E with 181 × 144 grids in the first layer and 208 × 175 grids in the second layer. The time step is set to 30s. For all twenty cases, the first 12 integration hours of each experiment are considered as the spin-up time. The FNL reanalysis data provide the initial and lateral boundary conditions of atmosphere to drive the model. The types of land surface within each model grid are obtained from the land-use classifications of MODIS (Friedl et al., 2010). The Smolarkiewicz method (SINT) (Kuo et al., 1999) is adopted for the horizontal interpolation in the drive data and the terrain-following coordinate system employs linear interpolation ($eta = \frac{P - P_{top}}{P_s - P_{top}}$).

According to the findings of Cai et al. (2021) and Huang & Gao (2018), the parameterization schemes adopted under different weather patterns are different, but the same parameterization schemes are adopted in multi-case simulations under the same weather pattern: (a) Under P1, the specific schemes are as follows: the Yonsei University planetary boundary layer scheme (Hong et al., 2006), the Morrison 2-moment microphysics scheme (Morrison et al., 2009), the CAM shortwave and longwave radiation schemes (Collins et al., 2004), the unified Noah land surface model (Tewari et al., 2004), and the Grell–Freitas ensemble cumulus parameterization scheme (Grell & Freitas, 2014). (b) Under P2, the specific schemes are as follows: the Asymmetric Convection Model 2 planetary boundary layer scheme (Pleim, 2007), the WRF Single–moment 3 class and 5 class microphysics scheme (Hong et al., 2004), the unified Noah land surface model (Tewari et al., 2004), the CAM shortwave and

21698996, 2025, 9, Downloaded from https://agupubs.onlinelibrary.wiley.com/doi/10.1029/2024JD042239 by Anming Huang - Nanjing University , Wiley Online Library on [28/04/2025]. See the Terms and Conditions (https://onlinelibrary.wiley.com/terms-and-conditions) on Wiley Online Library for rules of use; OA articles are governed by the applicable Creative Commons License

longwave radiation schemes (Collins et al., 2004), and the Grell–Freitas ensemble cumulus parameterization scheme (Grell & Freitas, 2014).

To investigate the impact of large-scale topography surrounding the SCB on its RHEPEs under two dominant weather patterns, The 3 groups of numerical experiments under each weather pattern are set as follows: the control experiment (called the CTL experiment) and two sensitivity experiments (called TP_N and YG_N). The CTL experiment adopts the real terrains (Figure 2a). The altitude of TP (27°N–40°N and 85°E–104.5°E) in the TP_N experiment is set to 500 m, which is the average elevation of SCB (Figure 2b). Analogously, the YG_N experiment sets the altitude of the YGP (22°N–28°N and 98°E–107°E) to 500 m (Figure 2c). Since this work adopts a two-way nesting strategy, terrain modifications have been made for the corresponding areas of D01 and D02. The delimiting of the region for TP and YGP is referenced in the previous research (Gu et al., 2020; Shi et al., 2017; Tang et al., 2018; Zhu et al., 2022). Based on the simulation results of 60 model runs (30 runs for each weather pattern), we explore the influence of large-scale topography on precipitation under the predominant weather patterns associated with the summer RHEPEs in SCB.

2.5. Methodology

The water vapor budget equation in this study is adopted to analyze the RHEPEs influenced by the terrain change (Li et al., 2020; Lin et al., 2014; Ma & Zhou, 2015). The original equation is as follows:

$$P = -\frac{\partial q}{\partial t} - \nabla \cdot \left(\vec{V}q\right) + E + \delta \tag{1}$$

Then

$$\nabla \cdot \left(\vec{V}q\right) = \frac{\partial (qu)}{\partial x} + \frac{\partial (qv)}{\partial y} + \frac{\partial (qw)}{\partial z} = \nabla_h \cdot \left(\vec{V}_h q\right) + \frac{\partial (wq)}{\partial z} \tag{2}$$

Let $< >$ equals to the $-\frac{1}{g}\int_{P_s}^{P_t} dp$, P_s, and P_t are respectively represent the surface and top layer pressure. Under the p coordinate system:

$$P = <\frac{\partial q}{\partial t}> + <\nabla_h \cdot \left(q\,\overrightarrow{V_h}\right)> + <\frac{\partial (\omega q)}{\partial p}> + E + \delta \tag{3}$$

The $q, \omega, g, \vec{V_h}$ symbolize the specific humidity, vertical velocity, acceleration of gravity, and wind vector respectively. Where P symbolizes the hourly precipitation rate, $\left\langle \frac{\partial q}{\partial t} \right\rangle$ signifies the changes in local water vapor with time, $\left\langle \nabla_h \cdot \left(q\,\overrightarrow{V_h}\right) \right\rangle$ is a horizontal water vapor flux convergence and $\nabla_h = \frac{\partial}{\partial x} + \frac{\partial}{\partial y}$, $<\frac{\partial (\omega q)}{\partial p}>$ describes the water vapor flux in vertical transport. The evaporation rate is represented by E, and δ is the residual term generated by the surface process which is connected with model bias and terrain.

The differences in the results between the CTL experiment and sensitive experiments are used to illustrate the influence of the terrain on the RHEPEs. The significance of the disparities is ascertained through the application of the t-test (Student, 1908).

3. Results

3.1. Model Evaluation

Figure 3 shows the distribution of mean situations of circulation at different levels and precipitation over SCB from the CTL experiment and observation under the two weather patterns of RHEPEs. Under P1, though the mean precipitation amount in the CTL experiment is weaker than the observation, the simulation results of the CTL experiment can well replicate the spatial distribution of the observed rainfall featured by the rainfall center concentrating on the western SCB. The spatial correlation coefficient between the precipitation simulated by the CTL experiment and observations is 0.56, with the significance at 0.01 level. Meanwhile, the CTL experiment reproduced the locations of SAH and WNPSH, though the strengths of SAH and WNPSH are slightly stronger

21698996, 2025, 9, Downloaded from https://agupubs.onlinelibrary.wiley.com/doi/10.1029/2024JD042239 by Aiming Huang - Nanjing University , Wiley Online Library on [28/04/2025]. See the Terms and Conditions (https://onlinelibrary.wiley.com/terms-and-conditions) on Wiley Online Library for rules of use; OA articles are governed by the applicable Creative Commons License

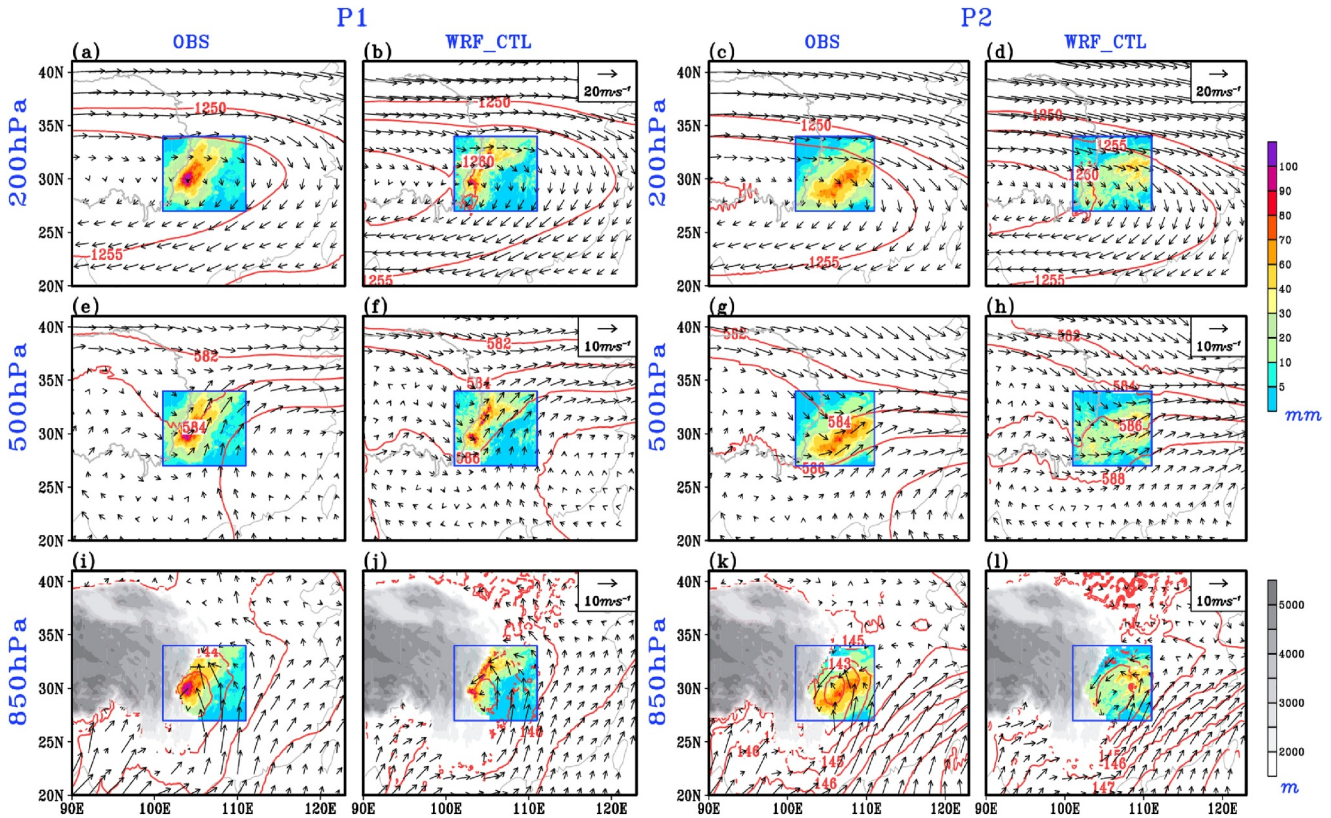

Figure 3. The spatial distribution of mean geopotential height (contour, unit: dagpm), wind (vector, unit: $m \cdot s^{-1}$) at 200, 500, and 850 hPa, and mean precipitation (shaded, unit: mm) under P1 (P2) from the observation and the CTL experiment. The circulation and precipitation observed data are from ERA5 and GPM IMERGE, respectively. The blue square indicates the position of the Sichuan Basin. The gray shadings indicate the terrain height.

than the observation (Figures 3a, 3b, 3e, and 3f). The LLV is precisely simulated by the CTL experiment with the location over the western SCB accompanied by the strong southerly winds under P1 (Figures 3i and 3j).

Under P2, the observed rainfall center located in the central-eastern SCB is reasonably reproduced by the CTL experiment. The spatial correlation coefficient between the CTL experiment simulated precipitation and observations is 0.41, which is at a significance of 0.1 level. Meanwhile, the location and intensity of SAH and WNPSH, the LLV, and the prevailing southwesterly winds are well reproduced in the CTL experiment (Figures 3c, 3d, 3g, 3h, 3k, and 3l). Overall, the multi-case simulations of the CTL experiment can reasonably reproduce the basic features of mean precipitation and atmospheric circulations over SCB in summer under different weather patterns of RHEPEs.

3.2. The Impact of Large-Scale Topography Surrounding the SCB on Its RHEPEs Under Different Weather Patterns

Under P1, the TP tends to intensify the rainfall in the western SCB (102°E–108°E and 29°N–33°N) where is the rainfall center of RHEPEs located (Figure 3a) with the rainfall regionally averaged over there increased by 86% (Figure 4a), while the existence of YGP can increase the regional mean rainfall over the region of the rainfall center of RHEPEs (102°E–108°E and 29°N–33°N) by 46% (Figure 4b). It is clear that the influence of YPG on the rainfall of RHEPEs under P1 is weaker than that of TP. Under P2, the existence of TP can increase the rainfall regionally averaged over the region of the rainfall center (104°E–110°E and 28°N–33°N) of RHEPEs shown in Figure 3c by 20% (Figure 4c), however, the existence of YGP can lead to the regional mean rainfall over the region of the rainfall center of RHEPEs decreased by 26% (Figure 4d). Overall, the TP tends to enhance the precipitation in the RHEPE rainfall center at different amplitudes under different weather patterns, but the YGP exhibits the opposite impact on the precipitation in the RHEPE rainfall center under different weather patterns.

21698996, 2025, 9, Downloaded from https://agupubs.onlinelibrary.wiley.com/doi/10.1029/2024JD042239 by Aiming Huang - Nanjing University , Wiley Online Library on [28/04/2025]. See the Terms and Conditions (https://onlinelibrary.wiley.com/terms-and-conditions) on Wiley Online Library for rules of use; OA articles are governed by the applicable Creative Commons License

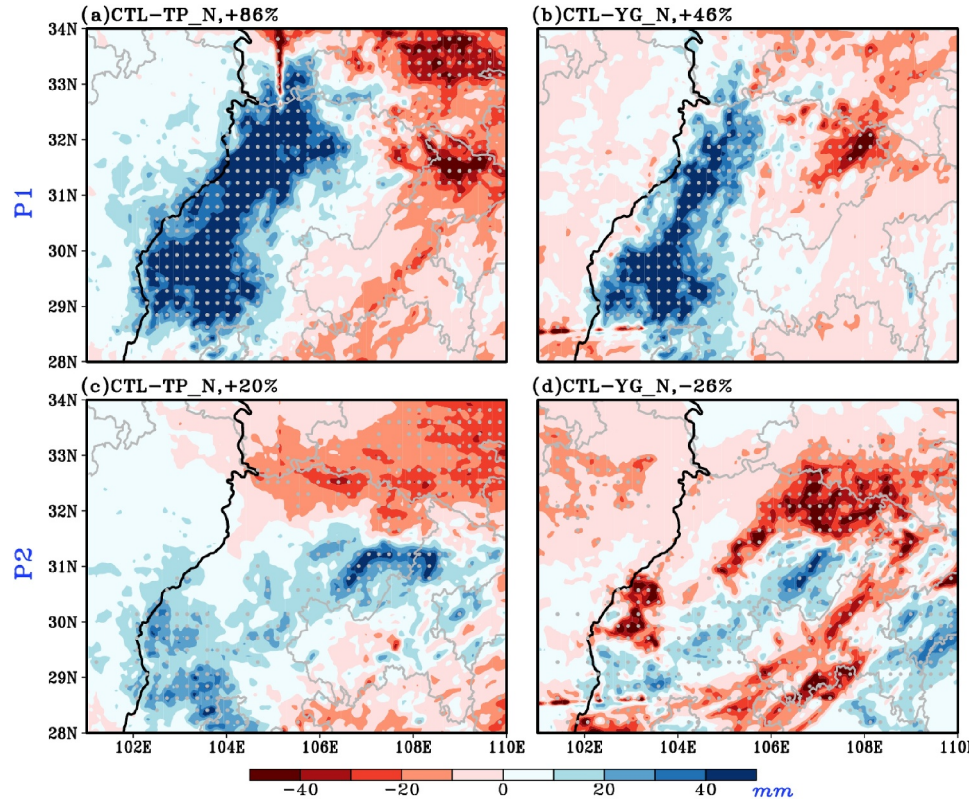

Figure 4. The difference in the mean precipitation between the CTL experiment and the sensitive experiment under P1 and P2, the numbers in the top of the left corner in the subplots represent the changes of the regional mean precipitation over the region of the rainfall center of regional hourly extreme precipitation events (102°E–108°E and 29°N–33°N under P1 in (a) and (b); 104°E–110°E and 28°N–33°N under P2 in (c) and (d)) in the CTL experiment relative to the sensitive experiment. The gray dots denote the statistical significance exceeding the 95% level of the *t*-test.

4. Possible Mechanisms

4.1. Water Vapor Budget Diagnosis

This chapter analyzes the main cause of the differences in the rainfall over the region of the rainfall center of RHEPEs mentioned above between the CTL experiment and each sensitivity experiment based on the water vapor budget equation. From Figure 5a, under P1, the difference in precipitation intensity *P* between the CTL experiment and the TP_N experiment indicates that the existence of TP increases the regional mean precipitation

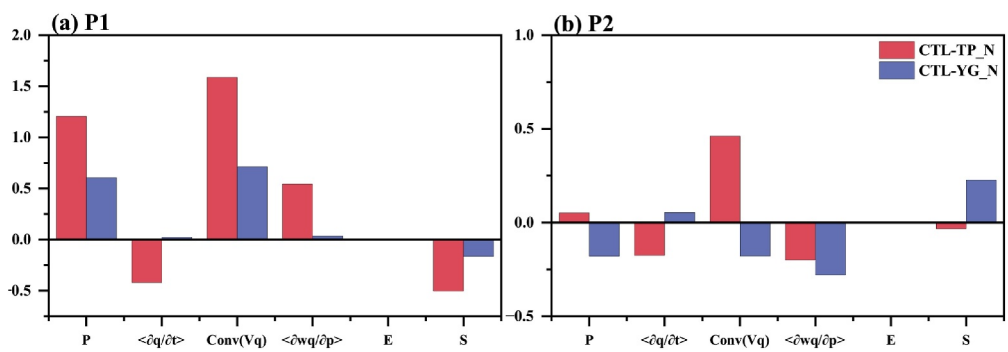

Figure 5. The difference in each component of the water vapor budget regionally averaged over the region of the rainfall center of the regional hourly extreme precipitation events (102°E–108°E and 29°N–33°N under P1; 104°E–110°E and 28°N–33°N under P2) between the CTL experiment and the sensitive experiment (unit: mm·h^{-1}).

21698996, 2025, 9, Downloaded from https://agupubs.onlinelibrary.wiley.com/doi/10.1029/2024JD042239 by Aiming Huang - Nanjing University , Wiley Online Library on [28/04/2025]. See the Terms and Conditions (https://onlinelibrary.wiley.com/terms-and-conditions) on Wiley Online Library for rules of use; OA articles are governed by the applicable Creative Commons License

intensity by 1.21 mm·h^{-1} relative to the situation without TP. The increased $Conv(Vq)$ with 1.59 mm·h^{-1} and enhanced $\langle \partial wq/\partial p \rangle$ with 0.54 mm·h^{-1} are the main causes of the increase of P under P1, indicating the strengthened large-scale water vapor convergence and strengthened local dynamic uplift effect induced by the existence of TP. Compared with the YG_N experiment, the existence of YGP increases the P by 0.61 mm·h^{-1} under P1, which is attributed to the strengthened large-scale water vapor convergence with the $Conv(Vq)$ increased by 0.71 mm·h^{-1}.

As shown in Figure 5b, under P2, the existence of TP increases the P regionally averaged over the rainfall center of RHEPEs (104°E–110°E and 28°N–33°N) by 0.05 mm·h^{-1}, which is much weaker than the situations under P1 (Figure 5a). It can be attributed to the water vapor convergence with the $Conv(Vq)$ increased by 0.46 mm·h^{-1} due to the existence of TP. The limited increased P under P2 compared with P1 can be explained by the weakened regionally mean dynamic uplift effect in the region of the 104°E–110°E and 28°N–33°N, which corresponds with the $\langle \partial wq/\partial p \rangle$ decrease of 0.28 mm·h^{-1} relative to the TP_N experiment under P2. The existence of YGP decreases the P by 0.18 mm·h^{-1} relative to the YG_N experiment under P2, which is attributed to the weakened large-scale water vapor convergence with the $Conv(Vq)$ decrease of 0.18 mm·h^{-1} and the weakened dynamic uplift effect with the $\langle \partial wq/\partial p \rangle$ decrease of 0.28 mm·h^{-1}.

In summary, the changes in the convergence of horizontal water vapor flux caused by large-scale circulation anomalies and the variation in vertical transport of water vapor flux caused by the local dynamic uplift effect of terrains are the main causes of mean precipitation differences between the CTL and sensitivity experiments under different weather patterns.

4.2. The Impact Mechanism of Large-Scale Topography on RHEPEs in SCB Under P1

In summer, the large-scale topography is a heat source absorbing more heat than the surrounding regions and warm advection is transmitted from the large-scale terrain to the surrounding region (Fu et al., 2019; Ge et al., 2019).

Under P1, with the barrier of TP, the large-scale topography of TP weakens the westerly winds and strengthens the anomalous southeasterly winds in the middle and upper layers over SCB (Figures 6a and 6c). The water vapor transports under P1 mainly come from the South China Sea transported by the southerly winds (Figure 1c). Therefore, compared with the TP_N experiment, the anomalous southeasterly winds with warm and wet air induce an increased temperature exceeding 2°C, increased specific humidity of 1.5 g·kg^{-1} and increased equivalent potential temperature (EPT) of ∼1.5 K over the western SCB in the CTL experiment, resulting in unstable atmosphere stratification and strengthened thermal uplift over SCB (Figures 6b and 6d). The existence of TP shapes the windward slope over the western SCB by inducing the anomalous LLV and strengthened southeasterly winds at 850 hPa over the western SCB (Figure 6e). Corresponding with the anomalous LLV relative to the TP_N experiment under P1, the local dynamic uplifting effect of terrain strengthens the upward motion by ∼−1.5 Pa·s^{-1} along the windward slope in western SCB (Figure 6f). Due to the existence of TP, the unstable atmosphere stratification (Figure 6b) and strengthened local dynamic uplifting effect of terrain along the windward slope in the western SCB (Figure 6f) lead to intensified precipitation there under P1 (Figure 6a). In addition, the existence of TP blocks the westerly winds and weakens the divergence of airflow at 200 hPa, thereby inhibiting the dynamic suction effect over northeastern SCB. Meanwhile, the anomalous LLV at 850 hPa located in western SCB weakens the transport of water vapor to the northeastern SCB (107°E–110°E and 31°N–34°N) due to existence of TP, ultimately leading to the decreased precipitation in this region (Figures 6a and 6e).

As the relatively smaller scale of YGP than TP, under P1, the influence of YGP on the atmospheric circulation at 200 hPa and 500 hPa is relatively weaker than the effect of TP (Figures 7a and 7c). However, the existence of YGP shapes the windward slope in the southwestern SCB by inducing the anomalous LLV over southwestern SCB, which strengthens the southeasterly winds over southern SCB under P1 (Figure 7e), leading to the air temperature increase of ∼1°C, specific humidity increase of 1.5 g·kg^{-1}, the EPT increase of ∼1.5 K, and the vertical velocity decrease of ∼−1.5 Pa·s^{-1} over western SCB and finally the intensified precipitation there (Figures 7b, 7d, and 7f).

21698996, 2025, 9, Downloaded from https://agupubs.onlinelibrary.wiley.com/doi/10.1029/2024JD042239 by Aiming Huang - Nanjing University , Wiley Online Library on [28/04/2025]. See the Terms and Conditions (https://onlinelibrary.wiley.com/terms-and-conditions) on Wiley Online Library for rules of use; OA articles are governed by the applicable Creative Commons License

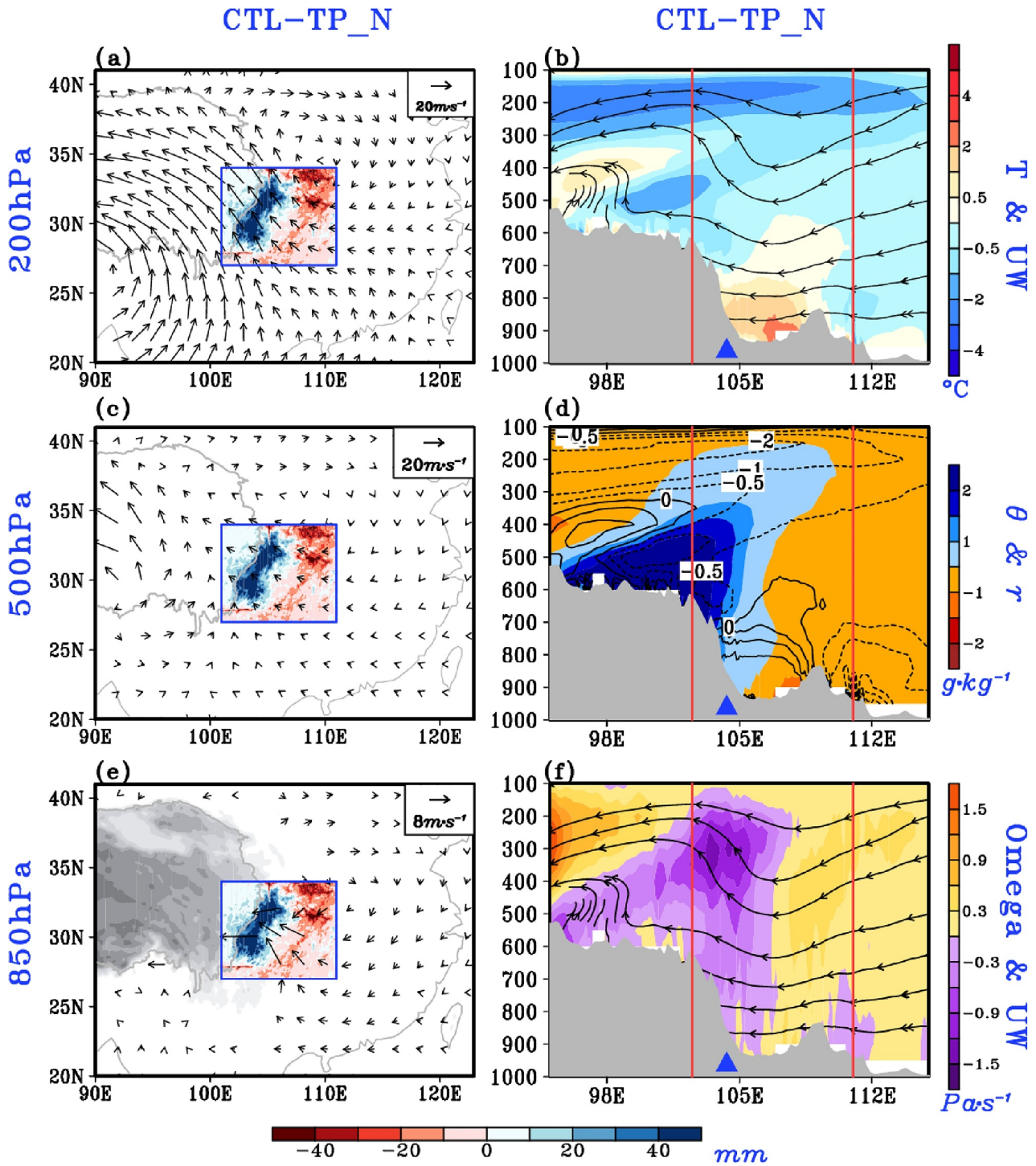

Figure 6. The spatial distribution of the differences in the mean winds (vector, unit: $m \cdot s^{-1}$) at the 200, 500, and 850 hPa and mean precipitation (shadings, unit: mm) between the CTL and TP_N experiments under P1. The blue squares in panels (a), (c), and (e) indicate the position of Sichuan Basin. The gray shading in panel (e) shows the topography in Tibetan Plateau. The height-longitude cross-section of the mean differences in the (b) air temperature (shaded, unit: ℃) and atmospheric circulation (stream); (d) specific humidity (shading, unit: $g \cdot kg^{-1}$) and equivalent potential temperature (contour, unit: K); (f) vertical velocity (shading, unit: $Pa \cdot s^{-1}$) and atmospheric circulation (stream) between the CTL experiment and TP_N experiment along 31°N under P1. The triangle denotes the center of precipitation difference in Figure 4a (blue represents the increase of precipitation; red represents the decrease of precipitation). The gray shadings in panels (b), (d), and (f) represent the topography profile.

21698996, 2025, 9, Downloaded from https://agupubs.onlinelibrary.wiley.com/doi/10.1029/2024JD042239 by Anming Huang - Nanjing University , Wiley Online Library on [28/04/2025]. See the Terms and Conditions (https://onlinelibrary.wiley.com/terms-and-conditions) on Wiley Online Library for rules of use; OA articles are governed by the applicable Creative Commons License

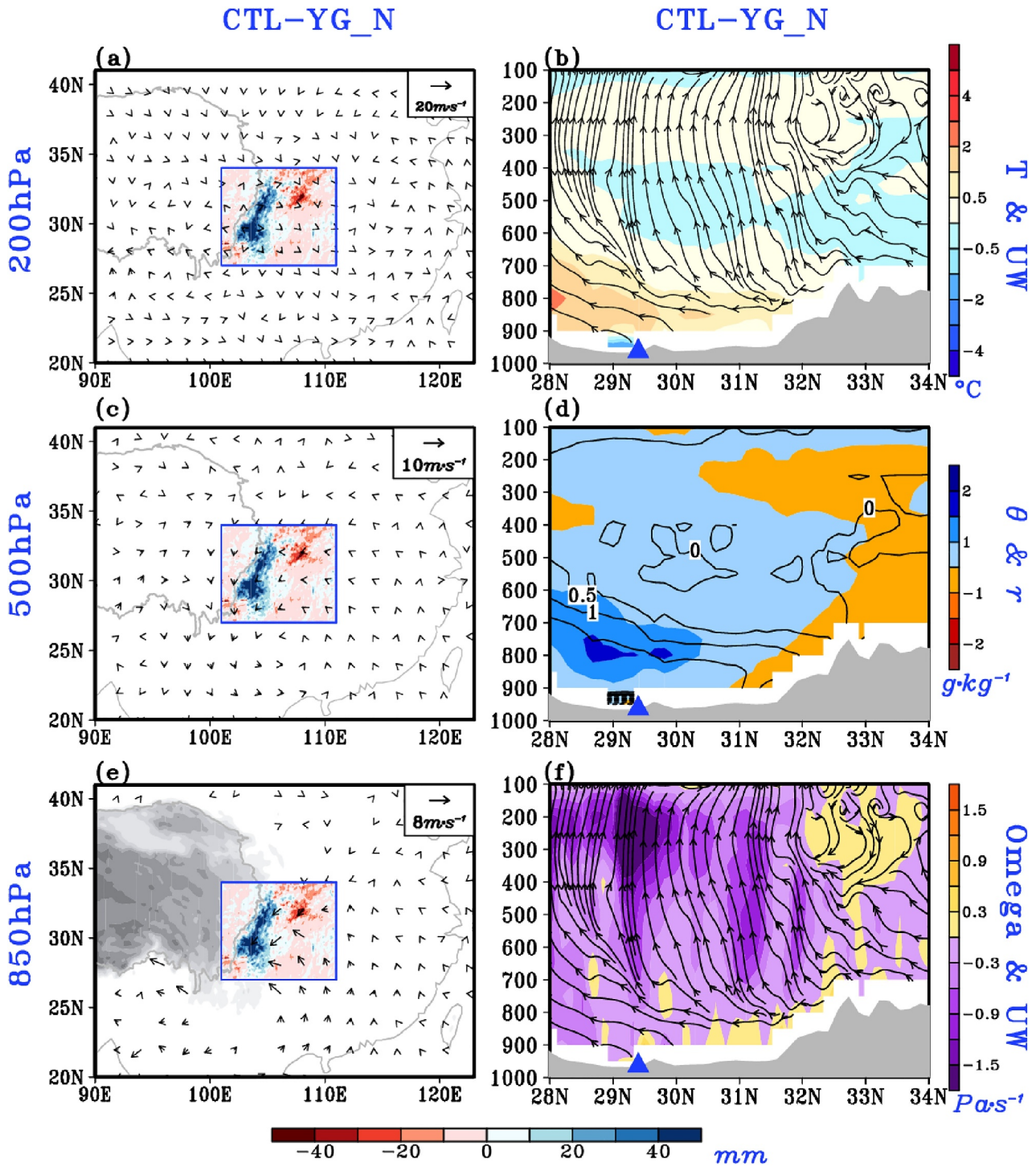

Figure 7. Same as Figure 6, but for the differences between the CTL experiment and the YG_N experiment, the height-latitude cross section of the differences along 104°E are shown in panels (b), (d), and (f).

4.3. The Impact Mechanism of Large-Scale Topography on RHEPEs in SCB Under P2

Under P2, the existence of TP strengthens the anomalous southeasterly winds at 200 hPa and 500 hPa, resembling the situations under P1 (Figures 8a and 8c). Nevertheless, the windward slope is situated in the eastern SCB, where the southwesterly winds facilitate the transport of water vapor (Figure 1b). The origin of southwesterly

21698996, 2025, 9, Downloaded from https://agupubs.onlinelibrary.wiley.com/doi/10.1029/2024JD042239 by Anming Huang - Nanjing University , Wiley Online Library on [28/04/2025]. See the Terms and Conditions (https://onlinelibrary.wiley.com/terms-and-conditions) on Wiley Online Library for rules of use; OA articles are governed by the applicable Creative Commons License

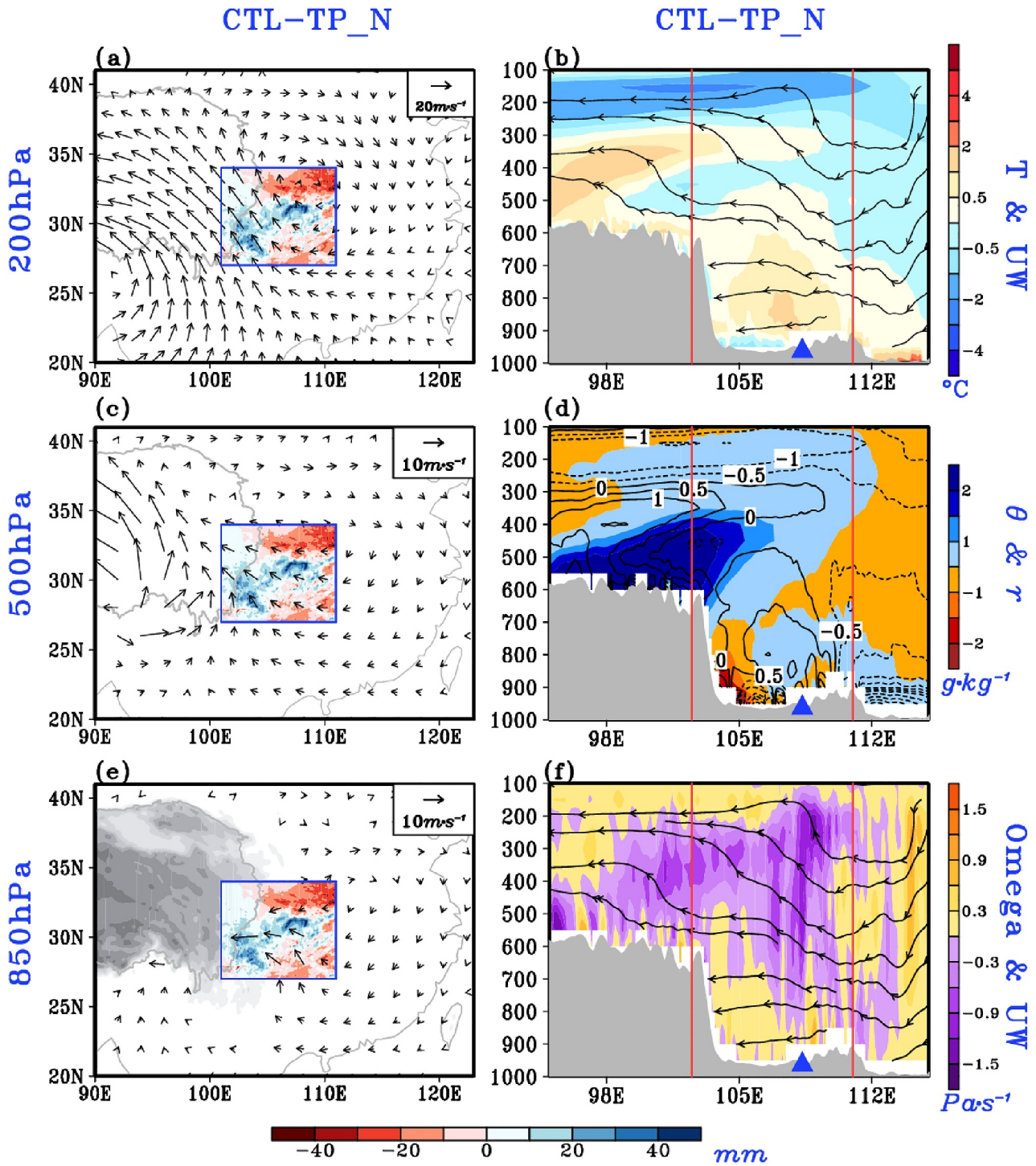

Figure 8. Same as Figure 6, but under P2.

winds under P2 is weakened by the anomalous southeasterly winds at 850 hPa induced by the existence of TP, resulting in less water vapor transport to the northeastern SCB (Figure 8e). Therefore, under P2, the existence of TP weakens the southerly winds at 850 hPa over northeastern SCB and reduces the water vapor transported into there. Moreover, the weakened southerly winds inhibit the uplifting effect of terrain on air over the northeastern SCB, leading to decreased precipitation there (Figure 8e). Meanwhile, the existence of TP under P2 induces the air temperature increase of ~0.5°C, specific humidity increase of ~1 g·kg^{-1}, EPT increase of ~1 K, and the

21698996, 2025, 9, Downloaded from https://agupubs.onlinelibrary.wiley.com/doi/10.1029/2024JD042239 by Aiming Huang - Nanjing University , Wiley Online Library on [28/04/2025]. See the Terms and Conditions (https://onlinelibrary.wiley.com/terms-and-conditions) on Wiley Online Library for rules of use; OA articles are governed by the applicable Creative Commons License

vertical velocity decrease of ~1.5 Pa·s^{-1} over the region of 104°E–108°E and 30°N–31°N, resulting in weakened precipitation there (Figures 4c, 8b, 8d, and 8f). The existence of TP has limited influence on the precipitation along the windward slope in the eastern SCB under P2 compared with the situations under P1. Consequently, the difference in vertical water vapor transport term of the water vapor budget equation between CTL and TP_N experiments regionally averaged over the region of 104°E–110°E and 28°N–34°N is negative under P2 (Figure 5b). In general, the increase of mean precipitation introduced by the existence of TP under P2 is less than that under P1.

Similar to the situations under P1, the existence of YGP has a limited influence on the atmospheric circulation at 200 and 500 hPa under P2 (Figures 9a and 9c). Under P2, YGP is located in the water vapor transport channel of RHEPEs in eastern SCB (Figure 1b). Under P2, the LLV is suppressed over the central and eastern SCB due to the existence of YGP, inducing anomalous northeasterly winds and weakened water vapor transport from the Bay of Bengal into SCB (Figure 9e). Subsequently, the suppressed LLV weakens the uplifting effect of terrain on air along the eastern edge of SCB, corresponding with an increased vertical velocity exceeding 1 Pa·s^{-1} in this region (Figures 9e and 9f). Concurrently, the decreased water vapor transport induced by the YGP is associated with the colder lower troposphere and warmer upper troposphere, suggesting a more stable atmospheric layer along the eastern edge of SCB (Figures 9b and 9d). Compared to the YG_N experiment, the CTL experiment produces the location of the precipitation center shifted to the eastern edge of SCB due to the coverage range of the LLV shrunk, leading to weakened rainfall in the region centered by the location of 107°E and 31°N in Figure 4d under P2 (Figure 9e).

5. Summary

This study selects multiple typical cases under two dominant weather patterns of summer RHEPEs in SCB and investigates the mechanism of large-scale topography surrounding SCB on RHEPEs. The main findings are as listed as follows:

Large-scale topography determines the occurrence and position of RHEPEs over SCB. Under P1 featured by an LLV over western SCB with southeasterly water vapor transport, the existence of TP and YGP can increase the precipitation in western SCB where the rainfall center of the RHEPE is located by 86% and 46%, respectively. The strengthened thermal uplift induced by the strengthened warm advection from surrounding large-scale terrain and the enhanced local dynamic uplifting effect of large-scale terrain on the windward slope over western SCB induced by the anomalous LLV at 850 hPa is the main causes for the increased precipitation over western SCB under P1 due to the existence of TP or YGP (Figures 10a–10c).

Under P2 featured by an LLV over the central and eastern SCB with southeasterly wind, the existence of TP can increase the rainfall center of RHEPEs (104°E–110°E and 28°N–33°N) in SCB by 20%. The anomalous southeasterly winds induced by the TP weaken the original southwesterly winds under P2 and have limited influence on the instability stratification and local dynamic uplift over eastern SCB, accounting for the precipitation along the windward slope in eastern SCB is less increased under P2 than under P1 (Figures 10d and 10e). However, the existence of YGP tends to decrease the rainfall over regions of the rainfall of RHEPEs under P2 by 26%, which is resulted from the anomalous northeasterly winds induced by the existence of YGP weakens the transport of water vapor from the Bay of Bengal, leading to the strengthened stability of stratification and weakened local dynamic uplifting effect of terrain along the windward slope over eastern SCB (Figures 10d and 10f).

This study provides a new perspective on the influence of topography on extreme precipitation by considering the mechanism of large-scale topography on RHEPE under different weather patterns. However, there are several limitations. For example, the precipitation is underestimated in the CTL experiment under P2, leading to large uncertainty in the amplitudes of the terrain effect on rainfall. In addition, the existing experimental design cannot accurately separate the thermal and dynamic effects of terrain. In future studies, further attempts can be made to close the sensible thermal process in the model to quantitatively explore the thermal and dynamic effects of large-scale terrain on the RHEPEs (Wang et al., 2016; Zhao, 2012). Based on the understanding of the influence mechanism of terrain on extreme precipitation, it is anticipated that the simulation performance of numerical models will be further improved.

21698996, 2025, 9, Downloaded from https://agupubs.onlinelibrary.wiley.com/doi/10.1029/2024JD042239 by Aiming Huang - Nanjing University , Wiley Online Library on [28/04/2025]. See the Terms and Conditions (https://onlinelibrary.wiley.com/terms-and-conditions) on Wiley Online Library for rules of use; OA articles are governed by the applicable Creative Commons License

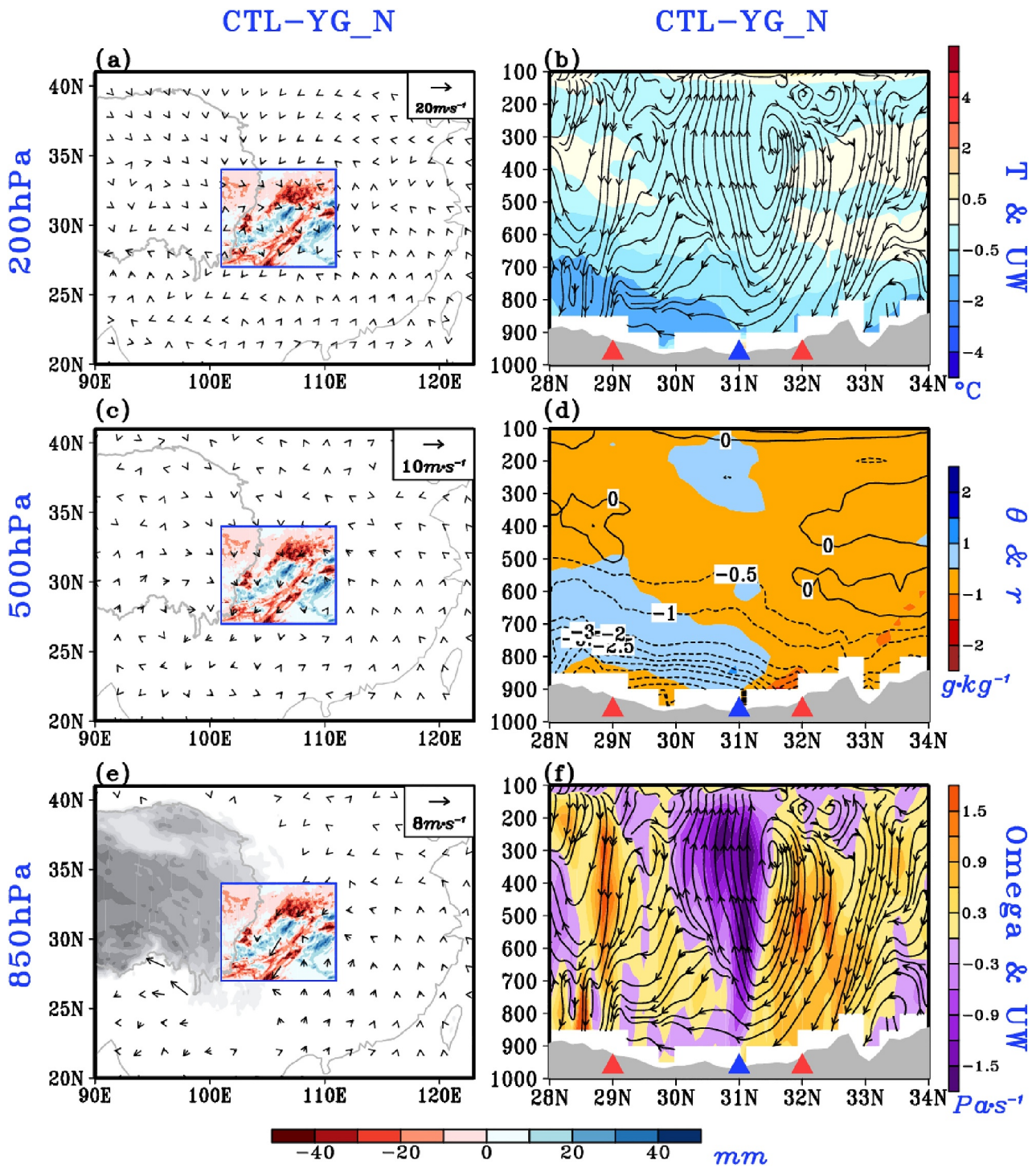

Figure 9. Same as Figure 7, but under P2. The height-latitude cross section of the differences along 107°E are shown in panels (b), (d), and (f).

21698996, 2025, 9, Downloaded from https://agupubs.onlinelibrary.wiley.com/doi/10.1029/2024JD042239 by Anming Huang - Nanjing University , Wiley Online Library on [28/04/2025]. See the Terms and Conditions (https://onlinelibrary.wiley.com/terms-and-conditions) on Wiley Online Library for rules of use; OA articles are governed by the applicable Creative Commons License

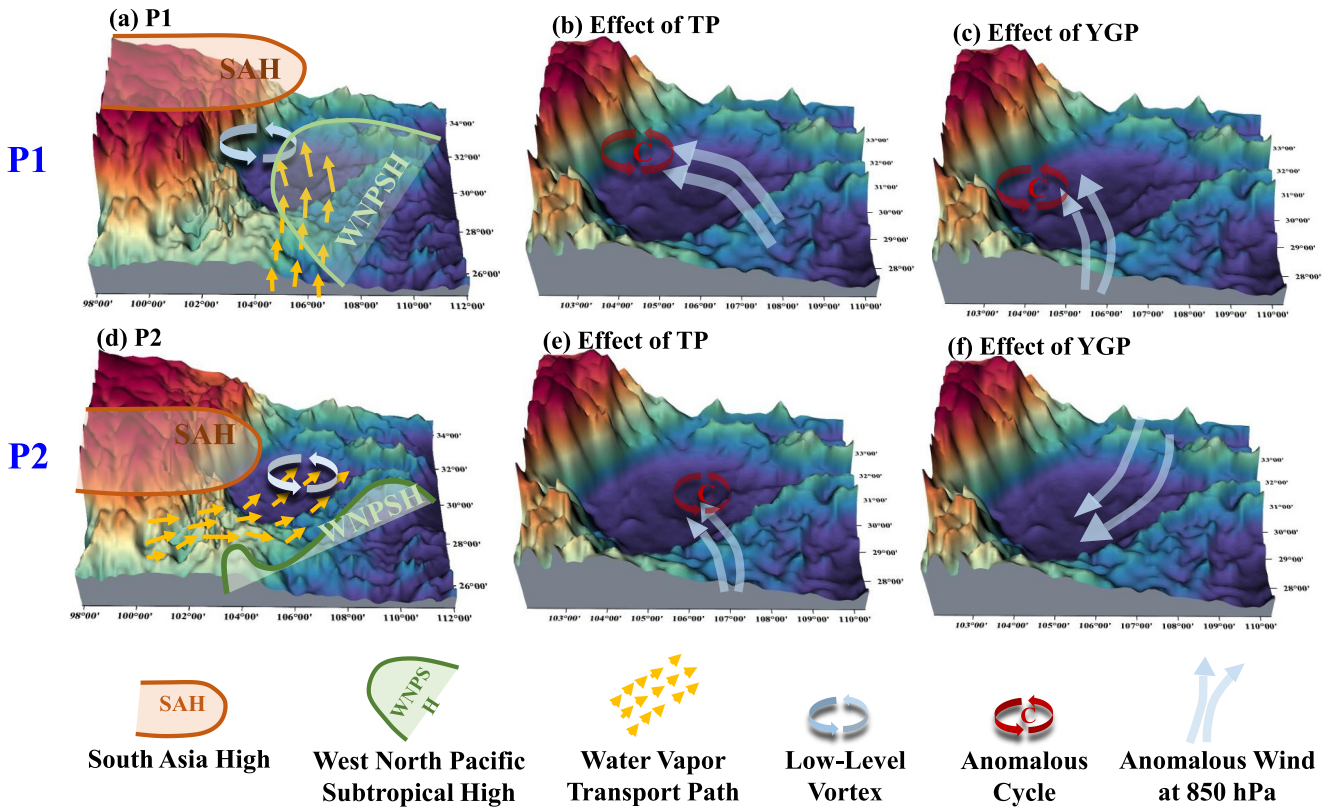

Figure 10. Illustrative diagram of the physical processes by which the Tibetan Plateau and Yunnan–Guizhou Plateau affect the regional hourly extreme precipitation events over Sichuan Basin in summer under different weather patterns. The elements in the figure are explained at the bottom. The water vapor transport path represents the vertically integrated water vapor flux from the surface to 300 hPa.

Data Availability Statement

The data set employed for this study is detailed below: (a) the GPM-IMERG precipitation data set, which has a spatial resolution of 0.1° (Hou et al., 2014). (b) The ERA5 reanalysis data set, characterized by a spatial resolution of 0.25°, is utilized in this study (Hersbach et al., 2020). (c) The data set from the National Centers for Environmental Prediction's final (FNL) global analysis, featuring a 2.5° horizontal resolution, is used in this research (National Centers for Environmental Prediction/National Weather Service/NOAA/U.S, 2000). (d) The numerical model (WRF) used in this study is version 4.2 (Skamarock et al., 2019).

Acknowledgments

This research is financially supported by the National Natural Science Foundation of China, with Grant U2342207, Open Research Fund Program of Plateau Atmosphere and Environment Key Laboratory of Sichuan Province (PAEKL-2023-K01), the CAS "Light of West China" Program (E129030101), the Jiangsu University "Blue Project" outstanding young teachers training object, and the Jiangsu Collaborative Innovation Center for Climate Change.

References

Almazroui, M., Raju, P. V. S., Yusef, A., Hussein, M. A. A., & Omar, M. (2018). Simulation of an extreme rainfall event of November 2009 over Jeddah, Saudi Arabia: The explicit role of topography and surface heating. *Theoretical and Applied Climatology*, *132*(1–2), 89–101. https://doi.org/10.1007/s00704-017-2080-2

Bao, X., Zhang, F., & Sun, J. (2011). Diurnal variations of warm-season precipitation east of the Tibetan Plateau over China. *Monthly Weather Review*, *139*(9), 2790–2810. https://doi.org/10.1175/MWR-D-11-00006.1

Cai, S., Huang, A., Zhu, K., Yang, B., Yang, X., Wu, Y., & Mu, X. (2021). Diurnal cycle of summer precipitation over the Eastern Tibetan Plateau and surrounding regions simulated in a convection-permitting model. *Climate Dynamics*, *57*(1–2), 611–632. https://doi.org/10.1007/s00382-021-05729-5

Chang, M., Liu, B., Martinez-Villalobos, C., Ren, G., Li, S., & Zhou, T. (2020). Changes in extreme precipitation accumulations during the warm season over continental China. *Journal of Climate*, *33*(24), 10799–10811. https://doi.org/10.1175/JCLI-D-20-0616.1

Chen, X., Zhang, F., & Zhao, K. (2016). Diurnal variations of the land–sea breeze and its related precipitation over South China. *Journal of the Atmospheric Sciences*, *73*(12), 4793–4815. https://doi.org/10.1175/JAS-D-16-0106.1

Cheng, X., Li, Y., & Xu, L. (2016). An analysis of an extreme rainstorm caused by the interaction of the Tibetan Plateau vortex and the Southwest China vortex from an intensive observation. *Meteorology and Atmospheric Physics*, *128*(3), 373–399. https://doi.org/10.1007/s00703-015-0420-2

21698996, 2025, 9, Downloaded from https://agupubs.onlinelibrary.wiley.com/doi/10.1029/2024JD042239 by Aiming Huang - Nanjing University , Wiley Online Library on [28/04/2025]. See the Terms and Conditions (https://onlinelibrary.wiley.com/terms-and-conditions) on Wiley Online Library for rules of use; OA articles are governed by the applicable Creative Commons License

Collins, W., Rasch, P. J., Boville, B. A., McCaa, J., Williamson, D. L., Kiehl, J. T., & Dai, Y. (2004). *Description of the NCAR community atmosphere model (CAM 3.0) (No. NCAR/TN-464+STR)*. University Corporation for Atmospheric Research. https://doi.org/10.5065/D63N21CH

Dong, Y., Li, G., Jiang, X., & Wang, Y. (2022). The characteristics and formation mechanism of double-band radar echoes formed by a severe rainfall occurred in the Sichuan Basin under the background of two vortices coupling. *Frontiers in Earth Science*, *10*, 915954. https://doi.org/10.3389/feart.2022.915954

Duan, A., Wu, G., Liu, Y., Ma, Y., & Zhao, P. (2012). Weather and climate effects of the Tibetan Plateau. *Advances in Atmospheric Sciences*, *29*(5), 978–992. https://doi.org/10.1007/s00376-012-1220-y

Fang, J., Yang, W., Luan, Y., Du, J., Lin, A., & Zhao, L. (2019). Evaluation of the TRMM 3B42 and GPM IMERG products for extreme precipitation analysis over China. *Atmospheric Research*, *223*, 24–38. https://doi.org/10.1016/j.atmosres.2019.03.001

Friedl, M. A., Sulla-Menashe, D., Tan, B., Schneider, A., Ramankutty, N., Sibley, A., & Huang, X. (2010). MODIS Collection 5 global land cover: Algorithm refinements and characterization of new datasets. *Remote Sensing of Environment*, *114*(1), 168–182. https://doi.org/10.1016/j.rse.2009.08.016

Fu, S. M., Mai, Z., Sun, J. H., Li, W. L., Ding, Y., & Wang, Y. Q. (2019). Impacts of convective activity over the Tibetan Plateau on plateau vortex, southwest vortex, and downstream precipitation. *Journal of the Atmospheric Sciences*, *76*(12), 3803–3830. https://doi.org/10.1175/JAS-D-18-0331.1

Fu, Y., Ma, Y., Zhong, L., Yang, Y., Guo, X., Wang, C., et al. (2020). Land-surface processes and summer-cloud-precipitation characteristics in the Tibetan plateau and their effects on downstream weather: A review and perspective. *National Science Review*, *7*(3), 500–515. https://doi.org/10.1093/nsr/nwz226

Ge, G., Shi, Z., Yang, X., Hao, Y., Guo, H., Kossi, F., et al. (2017). Analysis of precipitation extremes in the Qinghai-Tibetan plateau, China: Spatio-temporal characteristics and topography effects. *Atmosphere*, *8*(7), 127. https://doi.org/10.3390/atmos8070127

Ge, J., You, Q., & Zhang, Y. (2019). Effect of Tibetan Plateau heating on summer extreme precipitation in eastern China. *Atmospheric Research*, *218*, 364–371. https://doi.org/10.1016/j.atmosres.2018.12.018

Grell, G. A., & Freitas, S. R. (2014). A scale and aerosol aware stochastic convective parameterization for weather and air quality modeling. *Atmospheric Chemistry and Physics*, *14*(10), 5233–5250. https://doi.org/10.5194/acp-14-5233-2014

Gu, H., Yu, Z., Peltier, W. R., & Wang, X. (2020). Sensitivity studies and comprehensive evaluation of RegCM4. 6.1 high-resolution climate simulations over the Tibetan Plateau. *Climate Dynamics*, *54*(7–8), 3781–3801. https://doi.org/10.1007/s00382-020-05205-6

Hersbach, H., Bell, B., Berrisford, P., Hirahara, S., Horanyi, A., Munoz-Sabater, J., et al. (2020). The ERA5 global reanalysis [Dataset]. *Quarterly Journal of the Royal Meteorological Society*, *146*(730), 1999–2049. https://doi.org/10.1002/qj.3803

Hong, S. Y., Jimy, D., & Chen, Y. (2004). A revised approach to ice microphysical processes for the bulk parameterization of clouds and precipitation. *Monthly Weather Review*, *132*, 103–120. https://doi.org/10.1175/1520-0493(2004)132<0103:ARATIM>2.0

Hong, S. Y., Noh, Y., & Dudhia, J. (2006). A new vertical diffusion package with an explicit treatment of entrainment processes. *Monthly Weather Review*, *134*(9), 2318–2341. https://doi.org/10.1175/MWR3199.1

Hou, A. Y., Kakar, R. K., Neeck, S., Azarbarzin, A. A., Kummerow, C. D., Kojima, M., et al. (2014). The global precipitation measurement mission [Dataset]. *Bulletin of the American Meteorological Society*, *95*(5), 701–722. https://doi.org/10.1175/bams-d-13-00164.1

Hu, Y., Zhai, P., Liu, L., Chen, Y., & Liu, Y. (2015). Dominant large-scale atmospheric circulation systems for the extreme precipitation over the western Sichuan Basin in summer 2013. *Advances in Meteorology*, *2015*, 1–10. https://doi.org/10.1155/2015/690363

Hua, S., Xu, X., & Chen, B. (2020). Influence of multiscale orography on the initiation and maintenance of a precipitating convective system in north China: A case study. *Journal of Geophysical Research: Atmospheres*, *125*(13), e2019JD031731. https://doi.org/10.1029/2019JD031731

Huang, D., & Gao, S. (2018). Impact of different reanalysis data on WRF dynamical downscaling over China. *Atmospheric Research*, *200*, 25–35. https://doi.org/10.1016/j.atmosres.2017.09.017

Jin, X., Wu, T., & Li, L. (2013). The quasi-stationary feature of nocturnal precipitation in the Sichuan Basin and the role of the Tibetan Plateau. *Climate Dynamics*, *41*(3–4), 977–994. https://doi.org/10.1007/s00382-012-1521-y

Kuo, H. C., Leou, T. M., & Williams, R. T. (1999). A study on the high-order Smolarkiewicz methods. *Computers & Fluids*, *28*(6), 779–799. https://doi.org/10.1016/S0045-7930(98)00036-X

Li, J., Jiang, X., Schiemann, R., Chen, H., Li, Y., & Heng, Z. (2023). Prediction of the diurnal variation of summertime precipitation over the Sichuan Basin by a regional model. *Journal of Geophysical Research: Atmospheres*, *128*(2), e2021JD036247. https://doi.org/10.1029/2021JD036247

Li, L., & Zhang, R. (2023). Evolution mechanisms, impacts, and variations of the vortices originated from the Tibetan Plateau. *Earth-Science Reviews*, *242*, 104463. https://doi.org/10.1016/j.earscirev.2023.104463

Li, P., Furtado, K., Zhou, T., Chen, H., Li, J., Guo, Z., & Xiao, C. (2020). The diurnal cycle of East Asian summer monsoon precipitation simulated by the Met Office Unified Model at convection permitting scales. *Climate Dynamics*, *55*(1–2), 131–151. https://doi.org/10.1007/s00382-018-4368-z

Li, P., Yu, Z., Jiang, P., & Wu, C. (2021). Spatiotemporal characteristics of regional extreme precipitation in Yangtze River basin. *Journal of Hydrology*, *603*, 126910. https://doi.org/10.1016/j.jhydrol.2021.126910

Lin, R., Zhou, T., & Qian, Y. (2014). Evaluation of global monsoon precipitation changes based on five reanalysis datasets. *Journal of Climate*, *27*(3), 1271–1289. https://doi.org/10.1175/JCLI-D-13-00215.1

Liu, H., Huang, X., Fei, J., Zhang, C., & Cheng, X. (2022). Spatiotemporal features and associated weather patterns of extremely persistent heavy rainfall over China. *Journal of Geophysical Research: Atmospheres*, *127*(15), e2022JD036604. https://doi.org/10.1029/2022JD036604

Luo, Y., Wu, M., Ren, F., Li, J., & Wong, W. K. (2016). Synoptic situations of extreme hourly precipitation over China. *Journal of Climate*, *29*(24), 8703–8719. https://doi.org/10.1175/JCLI-D-16-0057.1

Ma, Q. R., Jia, F., Wu, X. X., Chang, Y. Z., Zhi, R., & Feng, G. L. (2022). Characteristics and related mechanisms of the persistent extreme precipitation in August 2020 over Western China. *Frontiers in Earth Science*, *10*, 1004612. https://doi.org/10.3389/feart.2022.1004612

Ma, S., & Zhou, T. (2015). Precipitation changes in wet and dry seasons over the 20th century simulated by two versions of the FGOALS model. *Advances in Atmospheric Sciences*, *32*(6), 839–854. https://doi.org/10.1007/s00376-014-4136-x

Morrison, H., Thompson, G., & Tatarskii, V. (2009). Impact of cloud microphysics on the development of trailing stratiform precipitation in a simulated squall line: Comparison of one- and two-moment schemes. *Monthly Weather Review*, *137*(3), 991–1007. https://doi.org/10.1175/2008MWR2556.1

National Centers for Environmental Prediction/National Weather Service/NOAA/U.S. Department of Commerce. (2000). NCEP FNL operational model global tropospheric analyses, continuing from july 1999 (Updated daily) [Dataset]. *Research Data Archive at the National Center for Atmospheric Research, Computational and Information Systems Laboratory*. https://doi.org/10.5065/D6M043C6

21698996, 2025, 9, Downloaded from https://agupubs.onlinelibrary.wiley.com/doi/10.1029/2024JD042239 by Anming Huang - Nanjing University , Wiley Online Library on [28/04/2025]. See the Terms and Conditions (https://onlinelibrary.wiley.com/terms-and-conditions) on Wiley Online Library for rules of use; OA articles are governed by the applicable Creative Commons License

Ng, C. P., Zhang, Q., & Li, W. (2021). Changes in hourly extreme precipitation over eastern China from 1970 to 2019 dominated by synoptic-scale precipitation. *Geophysical Research Letters*, *48*(5), e2020GL090620. https://doi.org/10.1029/2020GL090620

Nie, Y., & Sun, J. (2021). Synoptic-scale circulation precursors of extreme precipitation events over southwest China during the rainy season. *Journal of Geophysical Research: Atmospheres*, *126*(13), e2021JD035134. https://doi.org/10.1029/2021JD035134

Nielsen, E. R., Schumacher, R. S., & Keclik, A. M. (2016). The effect of the Balcones Escarpment on three cases of extreme precipitation in central Texas. *Monthly Weather Review*, *144*(1), 119–138. https://doi.org/10.1175/MWR-D-15-0156.1

Pan, H., & Chen, G. (2019). Diurnal variations of precipitation over North China regulated by the mountain-plains solenoid and boundary-layer inertial oscillation. *Advances in Atmospheric Sciences*, *36*(8), 863–884. https://doi.org/10.1007/s00376-019-8238-3

Plei m, J. E. (2007). A combined local and nonlocal closure model for the atmospheric boundary layer. Part I: Model description and testing. *Journal of Applied Meteorology and Climatology*, *46*, 1383–1395. https://doi.org/10.1175/JAM2539.1

Qian, C., Ye, Y., Zhang, W., & Zhou, T. (2022). Heavy rainfall event in mid-August 2020 in southwestern China: Contribution of anthropogenic forcings and atmospheric circulation. *Bulletin America Meteorology Social*, *103*(3), S111–S117. https://doi.org/10.1175/BAMS-D-21-0233.1

Qiao, P., Gong, Z., Liu, W., Zhang, Y., & Feng, G. (2022). Asymmetrical synchronization of extreme rainfall events in southwest China. *International Journal of Climatology*, *42*(11), 5935–5948. https://doi.org/10.1002/joc.7569

Shen, C., Li, G., & Dong, Y. (2022). Vertical structures associated with orographic precipitation during warm season in the Sichuan Basin and its surrounding areas at different altitudes from 8-year GPM DPR observations. *Remote Sensing*, *14*(17), 4222. https://doi.org/10.3390/rs14174222

Shi, Z., Sha, Y., & Liu, X. (2017). Effect of Yunnan–Guizhou topography at the southeastern Tibetan plateau on the Indian monsoon. *Journal of Climate*, *30*(4), 1259–1272. https://doi.org/10.1175/JCLI-D-16-0105.1

Shi, Z., Sha, Y., Liu, X., Xie, X., & Li, X. (2019). Effect of marginal topography around the Tibetan Plateau on the evolution of central Asian arid climate: Yunnan–Guizhou and Mongolian Plateaux as examples. *Climate Dynamics*, *53*(7–8), 4433–4445. https://doi.org/10.1007/s00382-019-04796-z

Skamarock, W. C., Klemp, J. B., Dudhia, J., Gill, D. O., Liu, Z., Berner, J., et al. (2019). A description of the advanced research WRF model version 4. [Softwere]. *National Center for Atmospheric Research*, *145*(145), 550. https://doi.org/10.5281/zenodo.10098038

Student. (1908). The probable error of a mean. *Biometrika*, *6*(1), 1–25. https://doi.org/10.2307/2331554

Sun, J., & Zhang, F. (2012). Impacts of mountain–plains solenoid on diurnal variations of rainfalls along the Mei-Yu front over the east China plains. *Monthly Weather Review*, *140*(2), 379–397. https://doi.org/10.1175/MWR-D-11-00041.1

Tang, G., Long, D., Hong, Y., Gao, J., & Wan, W. (2018). Documentation of multifactorial relationships between precipitation and topography of the Tibetan Plateau using spaceborne precipitation radars. *Remote Sensing of Environment*, *208*, 82–96. https://doi.org/10.1016/j.rse.2018.02.007

Tang, Y., Huang, A., Wu, P., Huang, D., Xue, D., & Wu, Y. (2021). Drivers of summer extreme precipitation events over East China. *Geophysical Research Letters*, *48*(11), e2021GL093670. https://doi.org/10.1029/2021GL093670

Tewari, M., Chen, F., Wang, W., Dudhia, J., LeMone, M. A., Mitchell, K., et al. (2004). Implementation and verification of the unified NOAH land surface model in the WRF model. In *20th conference on weather analysis and forecasting/16th conference on numerical weather prediction* (Vol. 1115(6), pp. 2165–2170).

Wang, Q. W., & Tan, Z. M. (2014). Multi-scale topographic control of southwest vortex formation in Tibetan Plateau region in an idealized simulation. *Journal of Geophysical Research: Atmospheres*, *119*(20), 11–543. https://doi.org/10.1002/2014JD021898

Wang, Z. Q., Duan, A. M., Li, M. S., & He, B. (2016). Influences of thermal forcing over the slope/platform of the Tibetan plateau on Asian summer monsoon: Numerical studies with the WRF model. *Chinese Journal of Geophysics*, *59*(5), 474–487. https://doi.org/10.1002/cjg2.30007

Wu, A., & Li, G. (2022). Roles of the topographically-affected boundary layer low-level jet in the moisture transport process of nocturnal rainstorms in mountainous areas around the western Sichuan Basin. *Atmosphere*, *14*(1), 84.

Wu, G., Duan, A., Liu, Y., Mao, J., Ren, R., Bao, Q., et al. (2015). Tibetan plateau climate dynamics: Recent research progress and outlook. *National Science Review*, *2*(1), 100–116. https://doi.org/10.1093/nsr/nwu045

Wu, Z., Liu, H., Chan, K. T., Wu, K., Zhang, W., & Wang, D. (2022). Effects of topography and latent heat on the evolution of a mesoscale dual-core southwest vortex over Sichuan Basin, China. *Frontiers in Earth Science*, *10*, 827601. https://doi.org/10.3389/feart.2022.827601

Xia, R., Luo, Y., Zhang, D. L., Li, M., Bao, X., & Sun, J. (2021). On the diurnal cycle of heavy rainfall over the Sichuan Basin during 10–18 August 2020. *Advances in Atmospheric Sciences*, *38*(12), 2183–2200. https://doi.org/10.1007/s00376-021-1118-7

Xu, H., & Yao, W. (2015). A numerical study of the Beijing extreme rainfall of 21 July 2012 and the impact of topography. *Advances in Meteorology*, *2015*, 1–12. https://doi.org/10.1155/2015/980747

Xu, X., Huang, A., Huang, D., Zhang, Y., Gu, C., Cai, S., et al. (2023). What are the dominant synoptic patterns leading to the summer regional hourly extreme precipitation events over central-eastern Tibetan plateau and Sichuan Basin? *Geophysical Research Letters*, *50*(5), e2022GL102342. https://doi.org/10.1029/2022GL102342

Xu, X., Huang, A., Zhao, W., Yang, B., Xue, D., & Zhang, Y. (2024). Roles of the Tibetan plateau and Yunna-Guizhou Plateau in the regional extreme precipitation over Sichuan Basin in summer: A case study. *Journal of Geophysical Research: Atmospheres*, *129*(3), e2023JD039776. https://doi.org/10.1029/2023JD039776

Yang, K., Chen, J., Lu, C., Li, J., Liu, T., Deng, L., & Li, Y. (2022). Impacts of regional uplift of the Tibetan plateau on local summer precipitation and downstream moisture budget: A simulation study. *International Journal of Climatology*, *42*(16), 8882–8903. https://doi.org/10.1002/joc.7781

Yang, K. Q., Xiao, D. X., Jiang, X. W., Li, Z. R., & Fu, S. M. (2023). Mechanisms governing the formation and long-term sustainment of a northeastward moving southwest vortex. *Sustainability*, *15*(12), 9255. https://doi.org/10.3390/su15129255

Yang, M., Liu, G., Chen, T., Chen, Y., & Xia, C. (2020). Evaluation of GPM IMERG precipitation products with the point rain gauge records over Sichuan, China. *Atmospheric Research*, *246*, 105101. https://doi.org/10.1016/j.atmosres.2020.105101

Zeng, J., Huang, A., Wu, P., Huang, D., Zhang, Y., Tang, J., et al. (2023). Typical synoptic patterns responsible for summer regional hourly extreme precipitation events over the middle and lower Yangtze River basin, China. *Geophysical Research Letters*, *50*(17), e2023GL104829. https://doi.org/10.1029/2023GL104829

Zhang, J., & Sun, X. (2021). Characteristics and cause analysis on a continuous severe rainstorm process in Sichuan Basin from August 10 to 14, 2020. (In Chinese). *Plateau and Mountain Meteorology Research*, *42*(3), 1674–2184.

Zhang, Y., Sun, J., Zhu, L., Tang, H., Jin, S., & Liu, X. (2021). Comparison of two types of persistent heavy rainfall events during sixteen warm seasons in the Sichuan Basin. *Atmospheric and Oceanic Science Letters*, *14*(6), 100094. https://doi.org/10.1016/j.aosl.2021.100094

21698996, 2025, 9, Downloaded from https://agupubs.onlinelibrary.wiley.com/doi/10.1029/2024JD042239 by Aiming Huang - Nanjing University , Wiley Online Library on [28/04/2025]. See the Terms and Conditions (https://onlinelibrary.wiley.com/terms-and-conditions) on Wiley Online Library for rules of use; OA articles are governed by the applicable Creative Commons License

Zhang, Y., Xue, M., Zhu, K., & Zhou, B. (2019). What is the main cause of diurnal variation and nocturnal peak of summer precipitation in Sichuan Basin, China? The key role of boundary layer low-level jet inertial oscillations. *Journal of Geophysical Research: Atmospheres*, *124*(5), 2643–2664. https://doi.org/10.1029/2018JD029834

Zhao, Y. (2012). Numerical investigation of a localized extremely heavy rainfall event in complex topographic area during midsummer. *Atmospheric Research*, *113*, 22–39. https://doi.org/10.1016/j.atmosres.2012.04.018

Zheng, Y., Gong, Y., Chen, J., & Tian, F. (2019). Warm-season diurnal variations of total, stratiform, convective, and extreme hourly precipitation over central and eastern China. *Advances in Atmospheric Sciences*, *36*(2), 143–159. https://doi.org/10.1007/s00376-018-7307-3

Zhu, D., Yang, Q., Xiong, K., & Xiao, H. (2022). Spatiotemporal variations in daytime and night-time precipitation on the Yunnan–Guizhou plateau from 1960 to 2017. *Atmosphere*, *13*(3), 415. https://doi.org/10.3390/atmos13030415

21698996, 2025, 9, Downloaded from https://agupubs.onlinelibrary.wiley.com/doi/10.1029/2024JD042239 by Aiming Huang - Nanjing University , Wiley Online Library on [28/04/2025]. See the Terms and Conditions (https://onlinelibrary.wiley.com/terms-and-conditions) on Wiley Online Library for rules of use; OA articles are governed by the applicable Creative Commons License